A numerical study of periodic disturbances on two-layer Couette flow

Jie Li, Yuriko Y. Renardy, and Michael Renardy

Citation: Physics of Fluids (1994-present) **10**, 3056 (1998); doi: 10.1063/1.869834
View online: http://dx.doi.org/10.1063/1.869834
View Table of Contents: http://scitation.aip.org/content/aip/journal/pof2/10/12?ver=pdfcov
Published by the AIP Publishing

A numerical study of periodic disturbances on two-layer Couette flow

Jie Li, Yuriko Y. Renardy, and Michael Renardy
Department of Mathematics and ICAM, Virginia Polytechnic Institute and State University, Blacksburg, Virginia 24061-0123

(Received 5 June 1998; accepted 17 August 1998)

The flow of two viscous liquids is investigated numerically with a volume of fluid scheme. The scheme incorporates a semi-implicit Stokes solver to enable computations at low Reynolds numbers, and a second-order velocity interpolation. The code is validated against linear theory for the stability of two-layer Couette flow, and weakly nonlinear theory for a Hopf bifurcation. Examples of long-time wave saturation are shown. The formation of fingers for relatively small initial amplitudes as well as larger amplitudes are presented in two and three dimensions as initial-value problems. Fluids of different viscosity and density are considered, with an emphasis on the effect of the viscosity difference. Results at low Reynolds numbers show elongated fingers in two dimensions that break in three dimensions to form drops, while different topological changes take place at higher Reynolds numbers. © *1998 American Institute of Physics.* [S1070-6631(98)00612-6]

I. INTRODUCTION

Flows composed of two immiscible liquids and undergoing shearing motions[1] can form fingers as a result of an interfacial instability due primarily to the viscosity jump. The jump in the viscosity from one fluid to the other results in the jump in the tangential velocity gradient across the interface, and can be thought of as a viscous counterpart of the Kelvin–Helmholtz instability. An example is Fig. 1 (courtesy of Fig. 20 of Ref. 2), where a cylinder is situated between the less viscous water below and more viscous oil above. As the cylinder begins to rotate, it brings with it a sheet of water. Observed from one end of the cylinder, the water–oil interface takes on a cusp-like structure. The sheet of water taken onto the cylinder then undergoes a three-dimensional instability, in the form of scallops along the length of the cylinder. At higher rotation rates, this leads to a fingering instability and then to emulsions of water droplets in oil foam. The experimental results[2] show fingering of certain low-viscosity liquids into high-viscosity liquids. Drops of low-viscosity liquid are torn off the fingertips, due to capillary instability, leading to the formation of an emulsion of low-viscosity drops in a high-viscosity foam. The drop formation from the fingers is similar to the breakup of jets into drops. Another motivation for this paper is that in coextrusion flow of very viscous liquids, the interface between the two fluids is often rippled.[3,4]

In this article, we attempt to capture the qualitative features of fingering by simulating two-layer Couette flow, which is one of the simplest of all the shearing flows of two fluids one might consider. A solution is shown in Fig. 2, where length is made dimensionless with respect to the plate separation. In dimensionless variables (x,y,z), the lower fluid is fluid 1 (with viscosity μ_1) and occupies $0<z<l_1$, and fluid 2 with viscosity μ_2 occupies $l_1<z<1$. There are four parameters: the viscosity ratio $m=\mu_1/\mu_2$, the average depth of the lower liquid l_1, the interfacial tension parameter $T=S^*/(\mu_2 U_i)$, where S^* is the interfacial tension coefficient, and U_i is the dimensional interfacial speed of the base flow, and a Reynolds number based on the lower fluid $R_1=U_i l^* \rho_1/\mu_1$, where l^* is the dimensional plate separation. With equal densities, gravitational force is balanced by a pressure gradient and can be neglected. The solution displayed in the figure has a base velocity field $[U(z),0]$, where

$$U(z)=\begin{cases} z/l_1, & 0\leqslant z\leqslant l_1, \\ (m/l_1)(z-1)+U_p, & l_1\leqslant z\leqslant 1, \end{cases} \tag{1}$$

where the dimensionless upper plate speed is $U_p=1+ml_2/l_1$, and the base pressure field is a constant. The stability of this solution has been addressed in Refs. 5, 6, and 7, for normal modes with wave number α in the flow direction and temporal dependence through $\exp(\sigma t)$. The two-layer Couette flow is a model problem that has received much analysis,[8] and has helped in the development of ideas about more complicated two-fluid flows. The problem has also attracted recent experimental results.[9]

In Couette flow, the fluid motion is mainly in the horizontal x direction. The analysis of stability of the state with a flat interface, and the subsequent development of weakly nonlinear waves serve as tests for our numerical codes. These theoretical works raise the following questions that we attempt to address in this paper: what is the range of validity for the linear theory, the weakly nonlinear theory, and what happens outside of this range? The first stage of fingering is a two-dimensional instability in the x-z plane, z being the vertical axis, which is different from the usual Saffman–Taylor instability associated with fingering in a Hele–Shaw cell, where the interface moves in the direction of the flow. In our case, depending on parameters, the interface moves mostly perpendicular to the flow direction, undergoing distortion. There is some analogy with the cusp-like structure of Fig. 1, in that the fingers in two dimensions are thin and long at the tips. The second stage is the development of three-dimensional scallop patterns in the direction transverse to the flow.

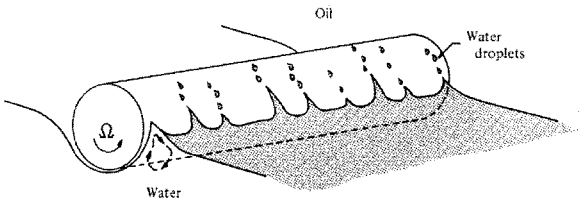

FIG. 1. Fingering instability leading to emulsions of water droplets in oil foam (Fig. 20 of Joseph, Nguyen and Beavers; Fig. 4.19 of Joseph and Renardy).

There are a number of algorithms one may pursue for the numerical simulation of interfacial instabilities in parallel shear flows of two fluids with different viscosities. We are further interested in predicting wave bending and breakup, past the point of pinch-off of drops, and we require a method that handles easily the breakup and reformation of interfaces. In this sense, the methods that have been used to predict liquid–liquid jet breakup are of relevance.[10] Examples include the front-tracking methods,[11,12] the level set method,[13] and volume tracking methods,[14–18] such as the volume of fluid (VOF) scheme. In this paper, we present results based on a VOF scheme.

The VOF method[19,20] is a fixed mesh approach to track the interface and uses a marker function convected by the flow. This allows for accurate interface advection and handles changes in interface topology. The application of the boundary conditions on the interface, however, is not straightforward. The CSF (continuous surface force) technique[21] has been developed to impose surface tension effects in an efficient manner. In this algorithm, interfacial tension forces are incorporated as body forces per unit volume in the momentum equations rather than as boundary conditions. This formulation is equivalent in the limit of infinitesimal interfacial thickness to the classical description of these forces as boundary conditions. A variation of the CSF algorithm is the CSS (continuous surface stress) technique,[15] in which the body force in the momentum equation is expressed as the divergence of a tensor, and hence the surface tension effects can be formulated in a conservative way. The problem of how to formulate these interfacial boundary conditions is, however, not completely solved. The loss of accuracy of these techniques may be serious, as observed in simulations of a spherical drop with surface tension:[21,15] the kinetic energy does not decay to zero but oscillates with constant amplitude, despite the physical and numerical dissipation. These are the so-called *spurious currents*, which pose a challenge for the numerical investigation of bubble motion. A better understanding of this numerical phenomenon is achieved in Ref. 22, where it is proved that the classical fixed mesh methods cannot admit a steady discrete solution similar to the one predicted by the Laplace Law (i.e., spherical interface shape, pressure jump equal to surface tension coefficient times the interface curvature) and hence *spurious currents* always exist for these methods. In fact, these methods mistreat the pressure near the interface. By taking into account the pressure jump explicitly in the numerical discretization,[22] a remedy is found for the front tracking method, where the interface is represented by marker points. Our pressure correction method is implemented in Ref. 23 and shown to effectively reduce *spurious currents* by a factor 10^5.

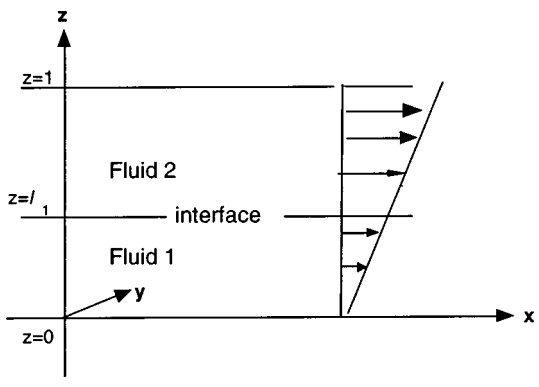

FIG. 2. Flow schematics.

The accuracy problem of CSF and CSS methods is less severe when investigating shear flow. It is easy to prove that these two methods model the surface tension effects well when the interface is a straight line parallel to a grid line (surface force nul in this case) and simulations of capillary waves in Ref. 24 show an error of 2% compared to theory.

The dynamic breakup of axisymmetric liquid–liquid jets[10] at first glance appears to be essentially the same as the two-layer Couette flow. However, the mechanisms that drive the unsteady motion are different: jet breakup is driven by surface tension, while interfacial evolution in the two-layer Couette flow is driven by the jump in shear rates across the interface. In Ref. 7, these issues necessitate the incorporation of the following to the code of Ref. 10. First, the physically correct viscosity interpolation in cells overlapping the interface is important. This need decreases if it is practical to implement a sufficiently small mesh size, which we have done in the present investigation. A second essential feature of our problem is that the interface shape propagates essentially as a traveling wave, with a deformation occurring on a much slower time scale. As a result of this, we achieved accuracy by introducing a Galilean transformation to a frame moving with the fluid on the interface. This is required in addition to the usual numerical stability conditions. Even with the Galilean transformation, Ref. 7 shows an unphysical formation of steps in the long term. In this paper, we succeed in removing these with a higher-order velocity interpolation scheme. It is found in Ref. 7 that the location where the first nonlinearity arises is the interfacial region. The interface and its neighboring region give birth to the nonlinearity while the bulk of the fluid behaves linearly, even for rather small initial amplitudes. The wave shapes found in Ref. 7 are qualitatively reminiscent of those seen in the experiments of Ref. 9 in a channel bent into an annular ring. In their experiments, they observed these shapes as saturated waves. Figure 3 shows a result from the code of Ref. 7, which was not able to reach saturation, for a qualitative comparison of the nonlinear wave forms. Their findings underscored the need for more accurate tracking of the interface, which motivates our present investigation.

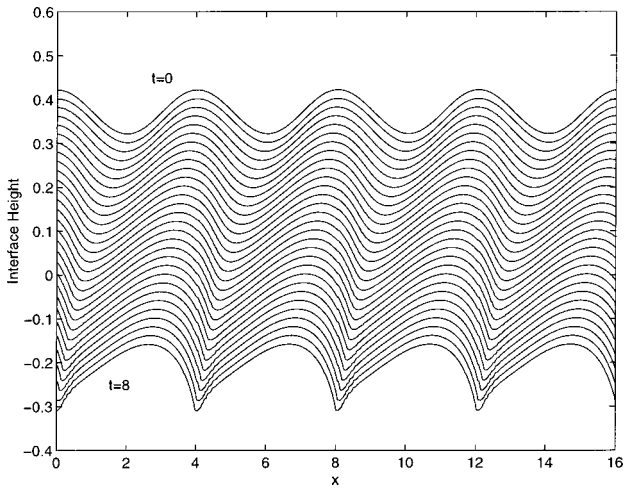

FIG. 3. Nonlinear wave steepening of the interface for $1 \leqslant t \leqslant 8$. The initial interface height is $z = 0.372 + 0.05\cos(\pi x/2)$, waves at subsequent time intervals are shifted down by 0.02, wave number $\alpha = \pi/2$, Reynolds number $R_1 = 500$ [Fig. 12(b) of Coward *et al.*].

Higher-order methods of interface representation are explored here. We begin with our code, which is derived from Refs. 15, 22, and 25 (Sec. I). The simulation of an inviscid Kelvin–Helmholtz instability has been obtained in Refs. 22 and 26 and our investigation is the viscous counterpart of this. With the explicit code, we foresee a problem for low Reynolds numbers, since the time steps must be small. This is addressed in Sec. II, where we institute a semi-implicit scheme that enables the use of larger timesteps and enhances computational efficiency.

In Sec. III, the question of how well the weakly nonlinear bifurcation analysis predicts saturation amplitudes is illustrated at sample situations. In particular, we pursue the computational work of Ref. 7 for viscosity ratio $m = 0.5$, and Reynolds numbers ranging from 40 to 500. The sat uration wave form and amplitudes are reproduced in the full numerical situation sufficiently close to onset, while nonlinear evolution and fingering are found farther away. The computations at low Reynolds numbers are related to the fingering results of Ref. 27 at large amplitudes for Stokes flow, and in addition, incorporate the effect of finite Reynolds numbers. In Sec. IV, the prediction of two dimensional (2-D) fingering with drop formation is presented. In Sec. V, the fingering is tracked farther into the 3-D regime.

A. The equations of motion

The two-fluid flow is modeled with the Navier–Stokes equation:

$$\rho\left(\frac{\partial \mathbf{u}}{\partial t} + \mathbf{u}\cdot\nabla\mathbf{u}\right) = -\nabla p + \nabla\cdot\mu\mathbf{S} + \mathbf{F}, \tag{2}$$

where ρ is the density, μ the viscosity, $\mathbf{S}$ the viscous stress tensor:

$$\mathbf{S}_{ij} = \frac{1}{2}\left(\frac{\partial u_j}{\partial x_i} + \frac{\partial u_i}{\partial x_j}\right),$$

and $\mathbf{F}$ the source term for the momentum equation. In our calculations, the body force $\mathbf{F}$ includes the gravity and interfacial tension force. Details are given in Refs. 15, 22, and 27. The velocity field $\mathbf{u}$ is subject to the incompressibility constraint:

$$\nabla\cdot\mathbf{u} = 0. \tag{3}$$

The two fluids are immiscible, and named fluids 1 and 2. Density and viscosity are constant in each phase but may be discontinuous at the interface. We use a volume fraction field C to represent and track the interface that is transported by the velocity field $\mathbf{u}$:

$$\frac{\partial C}{\partial t} + \mathbf{u}\cdot\nabla C = 0. \tag{4}$$

This equation allows for the calculation of density and viscosity. In fact, the average values of density and viscosity are interpolated by the following formulas:

$$\rho = C\rho_1 + (1-C)\rho_2, \tag{5}$$

$$\mu = C\mu_1 + (1-C)\mu_2. \tag{6}$$

B. Temporal discretization and projection method

The simultaneous solution of the large number of discrete equations arising from (2) and (3) is very costly, especially in three dimensions. An efficient approximation can be obtained by decoupling the solution of the momentum equations from the solution of the continuity equation by a projection method. The basic projection method was proposed by Chorin.[28] The MAC method proposed earlier by Harlow and Wesh[29] is a variant of that method.

In the present projection method, the momentum equations are first solved for an approximate $\mathbf{u}^*$ without the pressure gradient, assuming that $\mathbf{u}^n$ is known:

$$\frac{\mathbf{u}^* - \mathbf{u}^n}{\Delta t} = -\mathbf{u}^n\cdot\nabla\mathbf{u}^n + \frac{1}{\rho}\left[\nabla\cdot(\mu\mathbf{S}) + \mathbf{F}\right]^n. \tag{7}$$

In general, the resulting flow field $\mathbf{u}^*$ does not satisfy the continuity equation. However, we require that $\nabla\cdot\mathbf{u}^{n+1} = 0$ and

$$\frac{\mathbf{u}^{n+1} - \mathbf{u}^*}{\Delta t} = -\frac{\nabla p}{\rho}. \tag{8}$$

Taking the divergence of Eq. (8), we obtain

$$\nabla\cdot\left(\frac{\nabla p}{\rho}\right) = -\frac{\nabla\cdot\mathbf{u}^*}{\Delta t}, \tag{9}$$

which is used to find the pressure field. Next, $\mathbf{u}^*$ is corrected by this pressure field and the updated solution $\mathbf{u}^{n+1}$ is found from Eq. (8). This algorithm is easier to solve than the original fully coupled set of equations. We use two kinds of boundary conditions for the velocity: The periodic condition or the Dirichlet condition. Consistent with these boundary conditions for the velocity, the boundary condition for the pressure is periodic condition or Neumann condition, respectively.

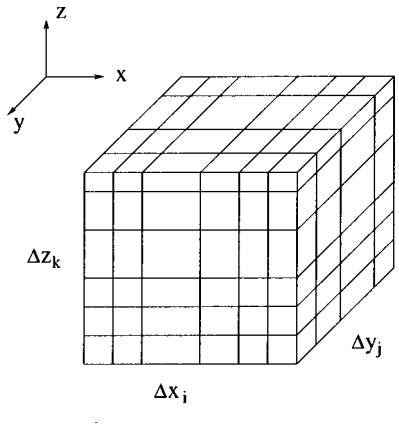

FIG. 4. A three-dimensional Cartesian mesh with variable cell sizes.

C. Spatial discretization

We use an Eulerian mesh of rectangular cells having variables sizes, Δx_i for the ith x-direction mesh size, Δy_j for the jth y-direction mesh size and Δz_k for the kth z direction mesh (Fig. 4). While not as flexible as a mesh composed of arbitrary quadrilaterals, the variable mesh capacity of our codes gives it a considerable advantage over methods using equal-size rectangles. For two-phase flows, in particular, the mesh can be refined in the interfacial region. The enormous memory and time consumption of three-dimensional simulations make this effort absolutely imperative. Navier–Stokes solvers for arbitrary mesh is now standard for the 3-D case;[30] however, the difficulty resides in the interface tracking. To our knowledge, there is no 3-D VOF method yet available for arbitrary mesh, although a 2-D code has been developed in Ref. 22.

The momentum equations are finite differenced on a locally variable, staggered mesh. As Fig. 5 shows, the x component of velocity $u_{i-1/2,j,k}$, the y component of velocity $v_{i,j-1/2,k}$ and the z component of velocity $w_{i,j,k-1/2}$ are centered at the right face, front face, and top face of the cell, respectively, whereas the pressure, $p_{i,j,k}$, and the volume fraction, $C_{i,j,k}$, are located at the center. This is the so-called MAC method. This apparently sophisticated mesh presents the advantage that in the resulting discrete Poisson equation, the pressure field is not decoupled and its solution permits no checkerboard oscillation. Another advantage of the MAC method is that the Neumann condition for the pressure is automatically involved in the numerical solution and is consistent with the Dirichlet condition for the velocity.[31] No numerical boundary condition is needed.

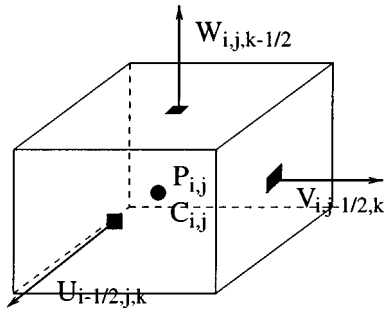

FIG. 5. The location of variables in a MAC mesh cell.

As reported by Hirt and Nichols,[20] the conservative scheme in a variable mesh loses one order of formal precision for the advective terms. Hence, we chose the nonconservative scheme; i.e.,

$$DUL=(u_{i-1/2,j,k}-u_{i-3/2,j,k})/\Delta x_{i-1},$$

$$DUR=(u_{i+1/2,j,k}-u_{i-1/2,j,k})/\Delta x_i,$$

$$\left(u\frac{\partial u}{\partial x}\right)_{i,j,k}=u_{i,j,k}\frac{\Delta x_i DUL+\Delta x_{i-1}DUR}{\Delta x_{i-1}+\Delta x_i}. \tag{10}$$

The basic idea in Eq. (10) is to weight the derivatives by cell size such that the correct order of approximation is maintained in a variable mesh. This type of approximation is used in our code for all convective terms appearing in Eq. (7).

The pressure and viscous terms in the momentum equation are calculated using second-order central finite differences, taking into account the variable mesh. The viscosity is calculated by formulas (6) once we know the volume fraction C. We should mention that contrary to the equal-size mesh, the discrete pressure equation is no longer symmetric. This can be seen from the $(\partial/\partial x)[(1/\rho)(\partial p/\partial x)]$ discretization:

$$\begin{aligned}\frac{\partial}{\partial x}\left(\frac{1}{\rho}\frac{\partial p}{\partial x}\right)_{i,j,k}&=\frac{1}{\Delta x_{i-1}}\left(\left(\frac{1}{\rho}\frac{\partial p}{\partial x}\right)_{i+1/2}-\left(\frac{1}{\rho}\frac{\partial p}{\partial x}\right)_{i-1/2}\right)\\&=-\frac{1}{\Delta x_i}\left[\frac{p_{i-1}}{\rho_{i-1/2}\delta x_{i-1/2}}-\left(\frac{1}{\rho_{i-1/2}\delta x_{i-1/2}}\right.\right.\\&\quad\left.\left.+\frac{1}{\rho_{i+1/2}\delta x_{i+1/2}}\right)p_{i,j,k}+\frac{p_{i+1}}{\rho_{i+1/2}\delta x_{i+1/2}}\right],\end{aligned} \tag{11}$$

where $\delta x_{i-1/2}=1/2(1/\Delta x_{i-1/2}+1/\Delta x_i)$. The discrete system is not symmetric because of the factor $1/\Delta x_i$.

The solution of the discrete counterpart of Poisson's equation (9) is the most time consuming part of our Navier–Stokes solver and, consequently, an efficient solution is crucial for the performance of the whole method. The performance of some classic iterative methods, such as the Gauss–Seidel method, the Cholesky incomplete factorization method, and the preconditioned conjugate gradient method suffer from the degradation of the convergence rate when the mesh size increases. Moreover, the system can be very ill conditioned when a large density ratio of the two fluids involved causes a sharp variation of the coefficients. Potentially, the multigrid method is the most efficient method: to reduce the error from a constant factor, the multigrid method needs a fixed number of iterations, whatever the mesh size. The multigrid method achieves this convergence rate independent of mesh size by combining two complementary algorithms: one iterative method to reduce the high-frequency error and one coarse grid correction step to eliminate the low-frequency error.

Our multigrid solver is derived from the one in Ref. 15, adapted to the variable mesh. As the discrete pressure is no

longer symmetric, new variables need to be declared. Furthermore, we use an algebraic approach (Galerkin method) instead of the physical one to find the coarse grid system. The algebraic approach can be generalized directly to the variable mesh case and provides also a better coarse grid correction. In Ref. 20, the algebraic approach is demonstrated at least five times more efficient than the physical one for rising bubble simulations, where the density ratio is the real ratio between water and air (about 1000). Two-color (for the 2-D case) and four-color (for the 3-D case) Gauss–Seidel methods are chosen as iterative methods, the periodic and Neumman boundary condition for the pressure necessitate no additional procedure during the numerical implementation. Their favorable convergence rates combined with a coarse grid correction makes the multigrid method one of the fastest solvers of the Poisson equation.

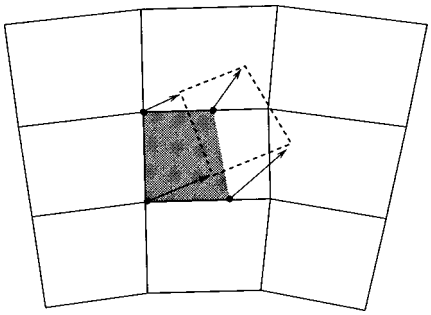

FIG. 6. The Lagrangian method on an arbitrary two-dimensional mesh. The shaded polygon represents the part occupied by the fluid in the central cell. The broken line shows the polygon position after advection in the local velocity field represented by arrows. The fluid is redistributed between neighboring cells, which the new polygon partially overlaps.

D. Piecewise linear interface calculation

The volume of fluid (VOF) method is especially suited to two-fluid shear flow simulations.[19,20,32–34] In this method, the location of the interface is approximately represented by the volume fraction C_{ij} of fluid 1 in the cell. We have $0<C<1$ in cells cut by the interface and $C=0$ or 1 away from it. For a review of this method, see Ref. 35.

Since we lose interface information when we represent the interface by a volume fraction field, the interface needs to be reconstructed approximately in each cell. The first-order VOF method of Ref. 7 shows an unphysical formation of steps in two-layer Couette flow at low speeds, close to onset conditions for traveling interfacial waves, and this underscored the need for higher-order methods. High-order methods have been, indeed, developed successfully by Refs. 22, 27, 35, and 36 both for 2-D and 3-D cases. Typically, the interface can be reconstructed by the piecewise constant (SLIC) or piecewise linear (PLIC) methods. When the latter method (the more accurate and more stable one) is chosen, the gist of interface reconstruction is to calculate the approximate normal $\mathbf{n}$ to the interface in each cell, since this determines one unique linear interface with the volume fraction of the cell. We find that discrete gradient of the volume fraction field provides a good approximation:

$$\mathbf{n}=\frac{\nabla^h C}{|\nabla^h C|}. \tag{12}$$

A least-square method[36] has also been implemented. This method improves the calculation of the interface normal, but no significant difference has been observed in the simulation of Couette flow.

The second step of the VOF method is to evolve the volume fraction field C. If the flow field is incompressible, i.e., $\nabla\cdot\mathbf{u}=0$, the advection equation can be recast in conservative form:

$$\frac{\partial C}{\partial t}+\nabla\cdot(\mathbf{u}C)=0. \tag{13}$$

A popular method is to apply an Eulerian scheme at this stage. In this case, the interface evolution is not governed by a conservative equation, and Eulerian schemes do not therefore preserve the physical constraint $0\leqslant C\leqslant 1$ on the volume fraction C. Hence, during the advection step, even with a sophisticated geometrical construction, there is a need to truncate the volume fraction C by the formula

$$C^{n+1}=\min[1,\max(C^{n+1},0)], \tag{14}$$

at the $(n+1)$th time step. Since interface evolution is governed by a transport equation, the Lagrangian method would appear more natural and more straightforward.[27,33] In this scheme, once the interface is reconstructed, the velocity at the interface is interpolated linearly and then the new position of the interface is calculated by the following formula:

$$\mathbf{x}^{n+1}=\mathbf{x}^n+\mathbf{u}(\Delta t). \tag{15}$$

Figure 6 illustrates how the Lagrangian method performs on an arbitrary two-dimensional mesh.[22]

On a Cartesian mesh, we can simplify the programming by an operator-split method: we reconstruct and advance the interface in each spatial dimension separately. Suppose that in box $[0,1]^2$ the interface segment is defined by a linear equation,

$$n_x x+n_y y=\alpha, \tag{16}$$

and the horizontal velocity defined on two vertical face centers are $u_{i-1/2,j}$ and $u_{i+1/2,j}$. Let A be a point on the above interface segment with coordinate (x,y). From linear interpolation we obtain its horizontal velocity:

$$u=(1-x)u_{i-1/2,j}+xu_{i+1/2,j} \tag{17}$$

and its updated coordinate x' at the $(n+1)$th time step, as defined in Eq. (15), is

$$x'=(1-u_{i-1/2,j}\Delta t+u_{i+1/2,j}\Delta t)x+u_{i-1/2,j}\Delta t, \tag{18}$$

where primes denote values at the $(n+1)$th step and variables without primes are evaluated at the nth time step. The new interface equation is still a linear equation:

$$n_x' x+n_y y=\alpha', \tag{19}$$

where

$$n_x'=n_x/(1-u_{i-1/2,j}\Delta t+u_{i+1/2,j}\Delta t),$$

and

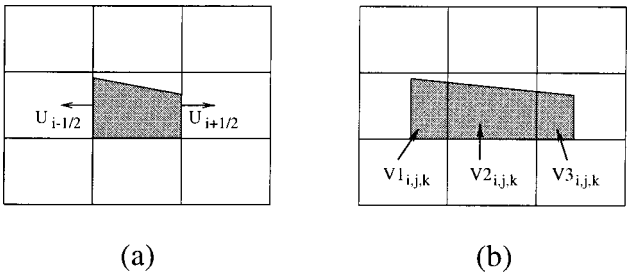

FIG. 7. The Lagrangian method during the advection step. (a) The shaded polygon represents the part occupied by the fluid in the central cell. (b) The contribution of this part to the new volume fraction field after advection.

$$\alpha' = \alpha + n_x' u_{i-1/2,j} \Delta t.$$

Figure 7 shows us how to obtain the new volume fraction from the new position of the interface. In Fig. 7(a), we suppose that $u_{i-1/2}<0$ and $u_{i+1/2}>0$. The part occupied by the fluid in the central cell is the shaded polygon. Figure 7(b) shows its new position calculated by Eq. (15). During the advection step, the central cell contributes $V1_{i,j,k}$ to the volume fraction of the left cell if $u_{i-1/2}<0$, $V3_{i,j,k}$ to the volume fraction of the right cell if $u_{i+1/2}>0$, and also $V2_{i,j,k}$ to the volume fraction of itself. $V1_{i,j,k}$ is the shaded area in the left cell and it is between the lines $x=u_{i-1/2}$, $y=0$, $x=0$ and Eq. (19). $V2_{i,j,k}$ and $V3_{i,j,k}$ can be calculated by the same manner. Thus, the new volume fraction $C_{i,j,k}$ in the cell (i,j,k) is

$$C_{i,j,k} = V3_{i-1} + V2_{i,j,k} + V1_{i+1}. \tag{20}$$

In a Lagrangian method, whenever the Courant condition $(\max|u|)\Delta t/h<1/2$ is satisfied, the algorithm is stable and satisfies the physical constraint $0 \leqslant C \leqslant 1$. Furthermore, the Lagrangian method is not subject to the incompressibility constraint. Figure 8 illustrates the example of a constant velocity field $\mathbf{u}=(1,0)$: (a) the interfaces in cells with volume fraction C are constructed; (b) the interface is advanced by Eq. (15) and the new volume fraction field is calculated from the new interface position; and (c) the interface is reconstructed from the new volume fraction field, and so on.

We should mention that until now our operator-split scheme is second-order accurate for the velocity field only in the advancing direction. It is only first-order accurate in the direction perpendicular to the advancing direction. While we have obtained good results for some kinematical tests (simple translation and solid rotation), it fails to be precise for shear flow. A simple shear velocity field in a box $[0,1]^2$ is $\mathbf{u}=(y,0)$. We initialize this with a sinusoidal wave on the interface [Fig. 9(a)], which is represented by the height function $z=0.5+0.05\cos(2\pi x)$. We can think of this simple test problem as modeling a limiting case of two-layer Couette flow at very low Reynolds numbers, with linear growth rates decreasing to zero, and resulting in only the deformation of the wave due to shear. Figure 9(b) shows the interface position at time $t=3$ calculated by the above Lagrangian method with a 64×64 uniform mesh. We observe that the interface wiggles behind the wave crest; the interface oscillates across grid lines. In this calculation, we have already improved the interface normal calculation by the least-squares method. The wiggle is not due to the calculation of the normal vector but due to poor approximation of velocity. In fact, the local horizontal velocity is defined at the vertical face center of cells. This results in a staggered movement of interface segments in cells at different horizontal levels; the velocity field presents a discontinuity across the grid lines [Fig. 10(a)]. Very fine mesh is needed for this method to improve velocity approximation and consequently eliminate interface wiggles. We remark that for this simple shear flow, our Lagrangian method is equivalent to the Eulerian method of Ref. 36.

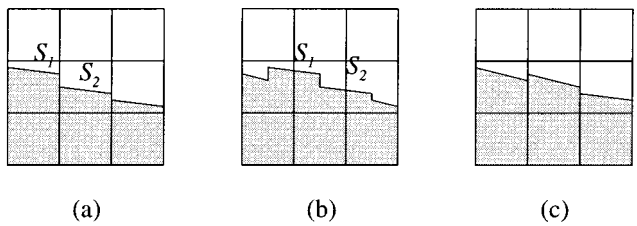

FIG. 8. An interface advected by the velocity field $\mathbf{u}=(1,0)$.

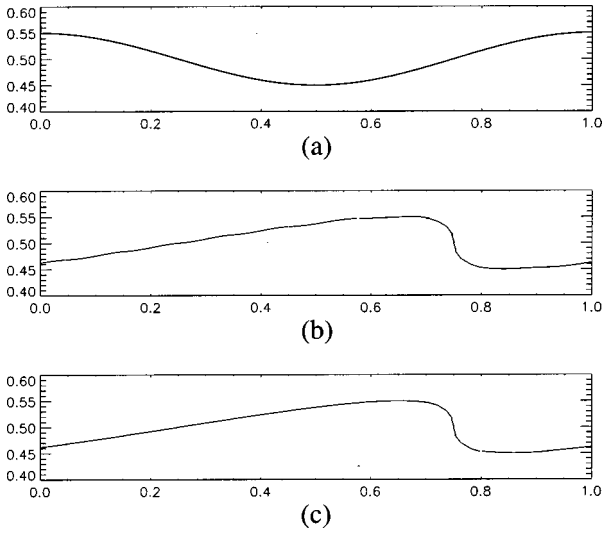

FIG. 9. (a) The initial interface height is $z=0.5+0.05\cos(2\pi x)$. (b) The interface position at time $t=3$ s calculated by the first-order velocity interpolation method. (c) The interface position at time $t=3$ s calculated by the second-order velocity interpolation method.

It is evident that we must make the velocity continuous across grid lines. Our strategy is to define the local velocity

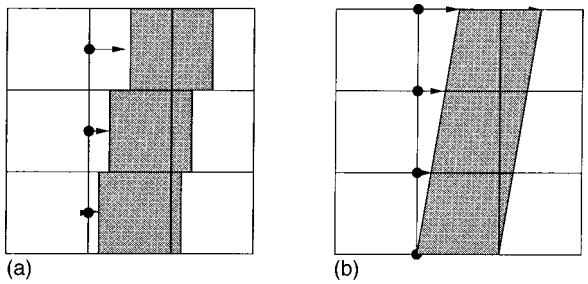

FIG. 10. (a) The first-order Lagrangian method. Local velocity is defined at the face center of the cell. The velocity field is discontinuous across the grid lines. (b) The second-order Lagrangian method. Local velocities are defined at corners of the cell. The velocity field is continuous across the grid lines.

on the four corners of the cell for the Lagrangian method. These velocities are obtained by linear interpolation and, consequently, the velocity approximation is second-order accurate in each direction. Figure 10 compares the first- and second-order Lagrangian methods. While in the first-order method the fluid moves with different velocities at different horizontal levels and fluid advection is discontinuous across grid lines, the second-order method reflects the shear property of the flow well and fluid advection is continuous across the grid lines. It is then not surprising that the second-order Lagrangian method eliminates the above wiggles of the interface. Figure 9(c) shows the interface position at time $t=3$ calculated by this method with a 64×64 uniform mesh; no oscillation of the interface is observed.

We have thus developed the PLIC method, both in two and three dimensions. This has been adapted by weighting the equation (20) by the mesh size for the variable mesh case.[37] Comparing to Ref. 7, we recover their findings for small amplitudes of interface perturbation, where the interface is nearly horizontal and the first-order VOF method is still reliable. In addition, we do not observe unphysical step formations when the interface undergoes large deformations.

II. SEMI-IMPLICIT STOKES SOLVER

When a VOF method is used, the boundary conditions at the interface are not applied directly, but replaced by some volume force formulation. As a consequence, a good resolution of the boundary conditions depends on the quality of the mesh. A fine mesh is usually required near the interface.

The use of a finer grid imposes, however, a further restriction on the time step size for the explicit method. Basically, given a mesh, the time scale for convective transport of a fluid particle to pass through a cell is

$$T_c=\min\left(\frac{\Delta x}{u},\frac{\Delta y}{v},\frac{\Delta z}{w}\right), \tag{21}$$

and the time scale of viscous diffusion for momentum to diffuse through a cell is

$$T_\mu=\frac{\rho h^2}{\mu}, \tag{22}$$

where h is the minimum of the mesh sizes $\min(\Delta x,\Delta y,\Delta z)$. The stability criterion for an explicit method is that the time steps Δt must be chosen less than the two above time scales: (i) the inviscid CFL (Courant–Friedrichs–Lewy) number $\Delta t/T_c<1$, and (ii) the Neumann number $\Delta t/T_\mu<1$.

As with any explicit method, simulations of very low Reynolds number flows are subject to strict stability limitations on the size of the time step and are therefore expensive. Furthermore, for tracking interfacial instabilities, fine grids need to be used near the interface. Since the viscous diffusion time scale $T_\mu\propto h^2$, this stability limit is hence much more restrictive than the CFL condition. For the physical parameters of Fig. 13 of Ref. 7 [$A(0)=0.01$, $\alpha=6.3$, $R_1=40$, $m=0.5$, $l_1=0.372$, $T=0.01$, equal densities, zero gravity], with a 160×1024 mesh, $T_\mu=2.39\times 10^{-8}$ and it is therefore impossible to run a code with a time step Δt less than this if we expect to perform a calculation for times of order 1. This makes the implicit treatment of the viscous terms imperative. Puckett and co-workers[36] developed a second-order scheme for the viscous terms. Their scheme possesses a full implicit part for the viscous terms and requires the solution of a coupled parabolic system for the velocity components. This system appears more complicated than the Poisson's equation and we presume that its solution would be comparable, if not more costly, to the solution of the pressure equation and therefore reduce the efficiency of the whole method. Our remedy for this dilemma is as follows.

The time integration scheme is constructed to be implicit for the Stokes operator, and otherwise explicit. Take the u component of the momentum equation (7), for example. This will be changed in the following way. We treat only the terms related to u (the terms with upper index $*$) implicitly and leave the other terms (the terms with upper index ^{n}) in the explicit part. Hence, this equation in the semi-implicit scheme is

$$\begin{aligned}\frac{u^*-u^n}{\Delta t}=&(\mathbf{u}^n\cdot\nabla)u^n+\frac{1}{\rho_n}F_1^n+\frac{1}{\rho^n}\frac{\partial}{\partial x}(2\mu^n u_x^*)\\&+\frac{1}{\rho^n}\frac{\partial}{\partial y}(\mu^n u_y^*+\mu^n v_x^n)+\frac{1}{\rho^n}\frac{\partial}{\partial z}(\mu^n u_z^*\\&+\mu^n w_x^n),\end{aligned} \tag{23}$$

and similarly for the v, w components. This can be expressed as

$$\begin{aligned}&\left\{I-\frac{\Delta t}{\rho}\left[\frac{\partial}{\partial x}\left(2\mu\frac{\partial}{\partial x}\right)+\frac{\partial}{\partial y}\left(\mu\frac{\partial}{\partial y}\right)+\frac{\partial}{\partial z}\left(\mu\frac{\partial}{\partial z}\right)\right]\right\}u^*\\&=\text{explicit terms.}\end{aligned} \tag{24}$$

This procedure decouples the u component from the above parabolic system. The same idea applies also to the other velocity components.

As far as the viscous terms are concerned, our semi-implicit scheme is unconditionally stable. The stability analysis can be carried out as follows (we will show only the 2-D case). Let $u\sim\exp(i\alpha x+i\beta y)$ and let $\mu=1$, $\rho=1$ for simplicity. Then

$$\begin{aligned}\begin{pmatrix}\dfrac{u^*-u^n}{\Delta t}\\[2ex]\dfrac{v^*-v^n}{\Delta t}\end{pmatrix}=&\begin{pmatrix}-2\alpha^2-\beta^2 & 0\\0 & -\alpha^2-2\beta^2\end{pmatrix}\begin{pmatrix}u^*\\v^*\end{pmatrix}\\&+\begin{pmatrix}0 & -\alpha\beta\\-\alpha\beta & 0\end{pmatrix}\begin{pmatrix}u^n\\v^n\end{pmatrix}\\&+\text{explicit terms},\end{aligned} \tag{25}$$

which reduces to

$$\begin{pmatrix} u^* \\ v^* \end{pmatrix} = \begin{pmatrix} 2\alpha^2+\beta^2+\dfrac{1}{\Delta t} & 0 \\ 0 & \alpha^2+2\beta^2+\dfrac{1}{\Delta t} \end{pmatrix}^{-1} \times \begin{pmatrix} \dfrac{1}{\Delta t} & -\alpha\beta \\ -\alpha\beta & \dfrac{1}{\Delta t} \end{pmatrix} \begin{pmatrix} u^n \\ v^n \end{pmatrix} + \text{explicit terms.} \tag{26}$$

The eigenvalues of the middle matrix above need to be less than $2\alpha^2+\beta^2+1/\Delta t$ and $\alpha^2+2\beta^2+1/\Delta t$. The eigenvalues are $1/\Delta t \pm \alpha\beta$. But $\alpha\beta$ are less than $\frac{1}{2}(\alpha^2++\beta^2)$. By a similar argument, we have also proved that our 3-D semi-implicit scheme is also unconditionally stable.

As the full explicit scheme, this semi-implicit scheme is first order in precision. Although it is more easy to be solved than the coupled system, it requires still inversions of a large sparse matrix. What makes the method very efficient is a factorization technique[30] that is applied to the left-hand side of Eq. (24):

$$\left\{I-\frac{\Delta t}{\rho}\left[\frac{\partial}{\partial x}\left(2\mu\,\frac{\partial}{\partial x}\right)\right]\right\}\left\{I-\frac{\Delta t}{\rho}\left[\frac{\partial}{\partial y}\left(\mu\,\frac{\partial}{\partial y}\right)\right]\right\} \times\left[I-\frac{\Delta t}{\rho}\frac{\partial}{\partial z}\left(\mu\,\frac{\partial}{\partial z}\right)\right]u^* = \text{explicit terms.} \tag{27}$$

It is easy to show that the error of the above factorization is of order $\mathcal{O}(\Delta t^3)$. The inversion of the left-hand side of Eq. (27) requires solving only tridiagonal matrices; this results in a significant reduction in computing and memory. In fact, the solution of these tridiagonal systems can be done in only $\mathcal{O}(N)$ operations (where N is the grid point number) and is insignificant compared to the solution of the pressure equation.

The efficiency of the above semi-implicit scheme is illustrated for the parameters of Fig. 13 of Ref. 7, given above for a 128×256 mesh. For the explicit run, we can merely take $\Delta t=10^{-4}$, the CFL$=1.27\times10^{-2}$, and the Neumann number $\Delta t/T_\mu=0.128$. In this calculation, the viscous diffusion time scale is much more restrictive than the convective transport one. For the implicit run, on the other hand, there is no restriction from the viscous diffusion time scale. We took $\Delta t=2\times10^{-3}$, the CFL$=0.254$, the Neumann number $\Delta t/T_\mu=2.56$. With the implicit scheme, we obtained the results of same quality as the explicit scheme, but we reduced the CPU by a factor of 20. We have seen that Eq. (24) is of order 1 and Eq. (27) is order 3, so the order of the whole scheme is of order 1.

The implicit scheme was run for our previous parameters on an extremely fine mesh (160×1024). As we are not subject to the viscous diffusion time scale, we chose our time step only according to the CFL number restriction, $\Delta t=2\times10^{-3}$, the CFL$=0.32$, and Neumann number $\Delta t/T_\mu=105$. This calculation took just a few hours on a SGI Onyx2 computer by using the above implicit scheme but will take more than two months if we use the explicit scheme. On the other hand, for low Reynolds number flow, coarse grid mesh is enough for a calculation far away from the interface. This advocates the use of a variable mesh size method.

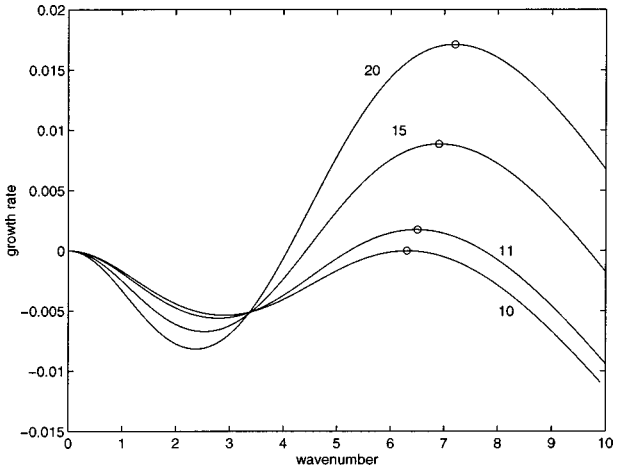

FIG. 11. Growth rate Re σ versus wave number α at $m=0.5$, $l_1=0.372$, $T=0.01$, equal density. Values of the Reynolds number are given next to each curve. The maximum growth rate points are circled. The approximate onset condition is $\alpha=6.3$, $R_1=10$.

III. SATURATION

At criticality, the two-layer Couette flow with a flat interface at $z=l_1$ loses stability to a Hopf bifurcation. The growth rate versus wave number plot is shown in Fig. 11 for viscosity ratio $m=0.5$, interfacial tension parameter $T=0.01$, equal densities, depth $l_1=0.372$. The maximum growth rate modes are circled. In the 2-D study of Ref. 7 and here, the initial condition is seeded with an eigenfunction derived from the linearized stability analysis of the base Couette flow.

The weakly nonlinear theory of Refs. 6 and 7 yields a Stuart–Landau equation for the amplitude function $Z(t)$ of the primary mode: $dZ/dt-\sigma Z=\kappa|Z|^2Z$, where κ denotes the Landau coefficient. The critical eigenfunction is denoted. ζ and the eigenvalue is denoted σ. The dynamics just above the onset of instability is dominated by the primary mode and its self-interactions. The traveling wave solution is predicted to saturate when the real part of the Landau coefficient is negative. The traveling wave solution is denoted $Z(t)=\exp(i\omega t)Z_0$ and substitution into the amplitude equation yields $i\omega Z_0-\sigma Z_0=\kappa|Z_0|^2Z_0$, or $i\omega-\sigma=\kappa|Z_0|^2$. Taking the imaginary part, we find the saturation amplitude to be

$$|Z_0|=\sqrt{-\text{Re }\sigma/\text{Re }\kappa}. \tag{28}$$

At our parameters, the results are tabulated in Table I. It is evident that the value of the Landau coefficient is approximately the same whether the pressure gradient is kept fixed (PG) or whether the volume flux is kept fixed (VF) throughout the weakly nonlinear analysis. Table I shows the theoretical saturation amplitudes $|Z_0|$ at the maximum growth rate points close to onset conditions. In addition, at $R_1=40$, $\alpha=6.3$, $\sigma=0.035-6.16i$, which was used in Ref. 7, $\kappa(\text{PG})=-133+602i$, $\kappa(\text{VF})=-133+588i$, and $|Z_0|=0.016$.

TABLE I. The Landau coefficients κ for the fixed pressure gradient (PG) and the fixed volume flux (VF), the wave number α of the maximum growth rate, the eigenvalue σ, and saturation amplitude Z_0, close to onset conditions. Here $m=0.5$, $l_1=0.372$, $T=0.01$, equal density.

R_1	α	σ	κ (PG)	κ (VF)	Z_0
11	6.5	$0.0017-6.43i$	$-218+1092i$	$-218+1074i$	0.0028
15	6.9	$0.0089-6.84i$	$-393+1250i$	$-393+1231i$	0.0047
20	7.2	$0.017-7.13i$	$-513+1253i$	$-513+1234i$	0.0058
40	7.5	$0.038-7.5i$	$-365+950i$	$-365+932i$	0.01

The wave shapes at saturation are represented as $z=l_1+\Phi_h$, where Φ_h is the perturbation solution comprised of the primary wave component h_ζ and the second harmonic h_η (notation as in Ref. 6):

$$\Phi_h=2\,\mathrm{Re}[Z_0 h_\zeta \exp(i\alpha x+\sigma t) + Z_0^2 h_\eta \exp(2i\alpha x+2\sigma t)]. \tag{29}$$

For the $R_1=11$ case, Fig. 12(a) shows the saturation wave form, and for the $R_1=15$ case, Fig. 12(b) shows the wave form. It is evident that the nonlinearity becomes important very quickly. Even the waves of Fig. 12(a) have lost the sinusoidal appearance and Fig. 12(b) shows two humps per wave. Comparing these, there is sensitivity in the shape as the situation moves off the onset case. The $R_1=15$ case is 50% above onset in the Reynolds number.

The asymptotic analysis shows that at $R_1=15$, $\alpha=6.9$, $l_1=0.327$, and $m=0.5$ the saturation will be reached at $A\approx 0.004$. Simulations of this length in duration at low Reynolds numbers would not have been possible without the use of the semi-implicit scheme for the viscous terms. Results for a variety of initial amplitudes below and over the predicted saturation amplitudes, $R_1=15$, $A(0)=0.003$, and $R_1=40$, $A(0)=0.01,0.05$ are shown to lead to fingering; see Sec. IV. Why is fingering preferred over wave saturation at these parameters? It is known that for Stokes flow,[27] the action of shearing an interface horizontally leads to elongation of an initial wave form to fingers. The low Reynolds numbers we address here would also show this phenomenon for sufficiently large initial waves. On the other hand, the finite Reynolds number affects the growth of waves through the linear instability due to viscosity stratification. The growth rate term originating from the viscosity stratification tends to zero as the Reynolds number tends to zero, while the interfacial tension term does not. The growth rate of the linear instability is proportional to the Reynolds number and is therefore small, but governs the vertical growth of the interface. The linear instability of the interfacial mode at, say, $\alpha=6.3$, $R_1=40$, involves a rather short wave and would therefore be confined to the interfacial region. The velocity field is only locally affected by the vertical linear growth rate for the interface position, and is overall affected more by the base Couette flow, favoring the fingering due to horizontal shearing at the interface, rather than the slow vertical growth to saturation. This is verified from our simulations, in which the maximum value of the velocity is attained some distance away from the interface.

In the experiments of Ref. 9, saturation is reached after a time of order 1000 s. The lower fluid is a water–glycerine (32%–68%) mixture with viscosity 0.0191 Pa s, density 1169 kg/m^3, and the upper fluid is mineral oil with viscosity 0.0297 Pa s, and density 846 kg/m^3. Interfacial tension is 0.03 Pa m. These experiments were conducted in a channel bent into a circular form, so that the base flow involves a slight centrifugal component. Nevertheless, this is modeled with two-layer Couette flow in Ref. 38, who used an upper plate velocity of 0.44 m/s, channel depth of 20 mm, and wavelength 6.8 cm, and depth of lower fluid 12.74 mm, to describe an onset condition. Under our notation,[6] the interfacial tension parameter is $T=S^*/(\mu_2 U_i)=3.14$, $F^2=U_i^2/(gl^*)=0.528$, where F is the Froude number, $R_1=U_i l^* \rho_1/\mu_1=394$, density ratio $r=\rho_1/\rho_2=1.3812$, viscosity ratio $m=\mu_1/\mu_2=0.645$, depth ratio $l_1=l_1^*/l^*=0.637$, dimensionless wave number $\alpha=1.9$. The weakly nonlinear results are shown in Table II. The amplitude $|Z_0|=0.007$ is equivalent to 0.14 mm.

The numerical investigation of saturation is difficult because the vertical motion of the interface crest is much smaller than the horizontal motion, and a relatively small

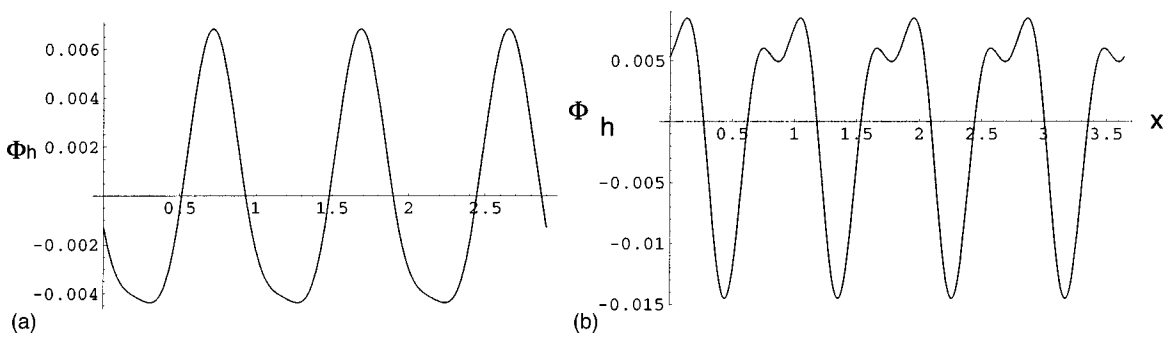

FIG. 12. The saturation wave form at $m=0.5$, $l_1=0.372$. (a) $\alpha=6.5$, $R_1=11$, $Z_0=0.0028$. (b) $\alpha=6.9$, $R_1=15$, $Z_0=0.005$.

TABLE II. The Landau coefficients κ for the fixed pressure gradient (PG) and the fixed volume flux (VF), the wave number α of the maximum growth rate, the eigenvalue σ, and the saturation amplitude Z_0, close to the onset conditions for mineral oil over the water/glycerine mixture.

R_1	α	σ	κ (PG)	κ (VF)	Z_0
394	1.9	$0.000\,38-1.05i$	$-7.82+24.8i$	$-6.63+28.9i$	0.007
500	1.9	$0.0068-1.05i$	$-9.14+27.4i$	$-7.3+32.6i$	0.03

error in the horizontal motion can feed back a significant error in the vertical motion. Linear theory predicts that the eigenvalue is $\sigma=3.7615\times10^{-4}-1.05i$. From the kinematic free surface condition, the complex vertical velocity is

$$v=h[\sigma+i\alpha U(l_1)]=h(3.7615\times10^{-4}+0.85i).$$

The interface shape is defined by

$$\mathrm{Re}(he^{i\alpha x})=h\ \cos(\alpha x).$$

This has one crest at $x=0$. Near this crest, the vertical velocity is

$$\mathrm{Re}(ve^{i\alpha x})=h[3.7615\times10^{-4}\ \cos(\alpha x)-0.85\ \sin(\alpha x)]$$
$$=h[3.7615\times10^{-4}-1.615x+\mathcal{O}(x^2)],$$

where the first term 3.7615×10^{-4} is much smaller than 1.615, and therefore a small error in the horizontal motion of the crest will result in a large error in its vertical motion. There are some sources of error that we can mention here. First, at $t=0$, the velocity and pressure we input are the base flow plus an eigensolution. The eigenfunction computed from the linear stability problem is defined over $0\leqslant l_1$ for fluid 1 and over $l_1\leqslant l_2$ for fluid 2. However, the domain occupied by fluid 1 is $0\leqslant l_1+h$ and that of fluid 2 is $l_1+h\leqslant 1$. To use the eigenfunction as an initial condition, we need to map it to the perturbed domain. Second, in our VOF discretization for the interface and MAC discretization for the velocity, boundary conditions are not taken into account explicitly, but treated as average quantities. Thus, a fine mesh is required to obtain precision. Our numerical investigation of the linear theory is presented in Table III, showing mesh convergence. We begin with a small initial amplitude $A(0)=10^{-5}$. The calculations have been done on different meshes with different time steps. We observe that increasing the y mesh number alone leads to significant improvement in the agreement with linear theory. For mesh 256×256, the error is 138.5%, and for mesh 256×2048 the error is 11.7%. The reduction of error is proportional to the y mesh number. The x mesh number and the time step size do not play an important role. Unfortunately, the excessive computational cost places a practical constraint on the computation with the larger mesh and for longer times.

We note that the evolution of bulk mode disturbances can be calculated accurately on a modest mesh. For example, the first bulk mode has a decay rate -0.1437. When the initial condition is seeded with this mode on a 256×256 mesh, the evolution of maximum of the interface height, the maximum of the vertical velocity V and L^2 norm against time are shown in Fig. 14. Very good agreement is obtained between linear theory and transient computations, the difference between the two is less than 1%.

The saturation of the flow with $R_1=394$ is investigated on a 256×256 mesh. Qualitative features of the flow are captured on this modest mesh. Figure 13 is the theoretical prediction for the saturated waves, with the same notation as in Fig. 12. Figure 15(a) illustrates the evolution of the interface amplitude versus time, showing saturation after a time of order 1000 s. The saturation amplitude is approximately 0.0175; the error in the saturation amplitude is of the same order as the error for the linear growth rate on this mesh. Figure 15(b) shows the simulated wave shape at 2500 s with flat crests and sharp troughs, in agreement with the weakly nonlinear theory. We conclude that the simulation at $R_1=394$ would require a finer mesh to resolve the evolution quantitatively.

At $R_1=500$, the growth rate is sufficiently high that the numerical resolution of the linear instability regime is relatively accurate on a 256×256 mesh. We obtain a linear growth rate 7.1×10^{-3} on this mesh, which yields a 4.41% error in comparison with linear theory. This simulation was started from a small initial amplitude in comparison with the expected saturation amplitude: $A(0)=0.0002$. The reason for choosing such a small initial amplitude is to initialize in the linear regime; otherwise, if the initial condition is already outside the linear regime, the solution may not saturate ac-

TABLE III. Linear growth rates calculated on different meshes and time steps. Here n_x is the x mesh number and n_y is the y mesh number; $R_1=394$. The theoretical growth rate is 3.7615×10^{-4}.

$A(0)$	n_x	n_y	Δt	Numerical growth rate	Error
10^{-5}	256	256	10^{-4}	8.97×10^{-4}	138.5%
10^{-5}	514	256	10^{-4}	9.13×10^{-4}	142.8%
10^{-5}	1024	256	10^{-5}	9.17×10^{-4}	143.9%
10^{-5}	256	512	10^{-4}	6.12×10^{-4}	63.8%
10^{-5}	512	512	10^{-4}	6.28×10^{-4}	67.0%
10^{-5}	256	1024	10^{-4}	4.80×10^{-4}	27.5%
10^{-5}	256	2048	10^{-4}	4.160×10^{-4}	10.5%

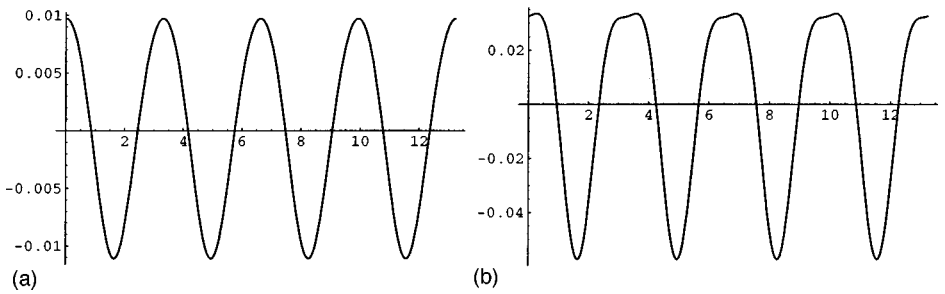

FIG. 13. The saturation wave form for parameters of Table II. (a) $R_1=394$. (b) $R_1=500$.

cording to weakly nonlinear theory. The Log plot of the maximum of interface height versus time is shown in Fig. 16(a), the flow is in the linear regime during the first 700 s. The evolution of the maximum of the interface height is shown in Fig. 16(b); the saturation amplitude we obtained is approximately 0.031, in good agreement with the weakly nonlinear theory. Finally, the interface height at $x=0$ is shown in Fig. 16(c). We mention that when the flow reaches saturation, our VOF scheme begins to lose some mass on this mesh. A finer mesh is needed to reduce this deficiency.

IV. FINGERING IN TWO DIMENSIONS

Our ultimate objective is the study of 3-D effects. Three-dimensional simulations are, however, limited by the machine memory and computation time. As our flow manifests a quasi-two-dimensional behavior in the early stages and the three-dimensional effects come later, preliminary two-dimensional studies are necessary, because they can provide useful information for our choices of physical and numerical parameters. We study in this section the large-amplitude perturbation of two-layer Couette flow depicted in Fig. 2. This flow is subjected to a periodic perturbation that disturbs the interface and the velocity field in a sinusoidal manner with amplitude $A(0)$. In this section, the densities of the two fluids are assumed to be the same and so the gravity does not play a role. Furthermore, we suppose that the undisturbed interface height is $l_1=0.372$ and the viscosity ratio of the fluids is $m=0.5$. Linear theory predicts that, as long as the amplitude is sufficiently small, a sinusoidal perturbation to the Couette flow with an appropriate wave number grows exponentially. This tendency to grow vertically competes with the convective action of the simple shear flow to distort the interface. For the higher amplitudes of perturbation, the dominant tendency is the horizontal shift on the crests and troughs. When the perturbation amplitude is large enough, the folding of the interface under the shear simple flow convection is so important that the linear theory fails to predict the flow evolution. Beyond the linear growth region, although the weakly nonlinear theory is relevant in many cases, there is much that happens at low Reynolds numbers at seemingly small amplitudes, which lead to nonlinear processes that must be simulated numerically.

First, we investigate the flow with $m=0.5$, equal density, $T=0.01$, Reynolds number $R_1=500$, and wave number $\alpha=\pi/2$. This was examined for short times in Ref. 7 and we pursue these parameters for longer times. Linear theory indicates the growth rate is $\mathrm{Re}(\sigma)=0.035\,77$ for this flow. We

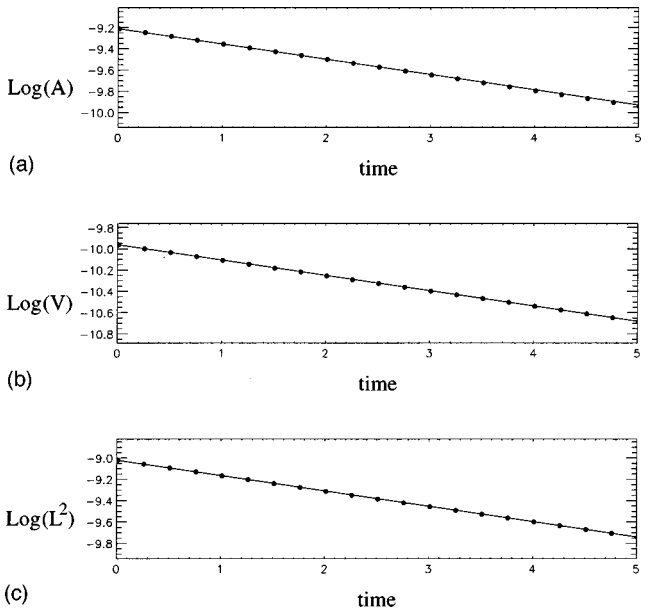

FIG. 14. The log plot of the maximum of interface height (a), the log plot of the maximum of vertical velocity (b), and the log plot of the L^2 norm against time (c) for the flow: $A(0)=0.0001$, $\alpha=1.9$, $R_1=394$, $m=0.646\,15$, $l_1=0.636\,94$, $T=3.14$, density ratio. Linear stability analysis indicates that the growth rate for the bulk mode is -0.1437. Solid lines represent theory and circles represent the numerical calculation. The difference is less than 1%. The calculation is carried out on a 256×256 mesh.

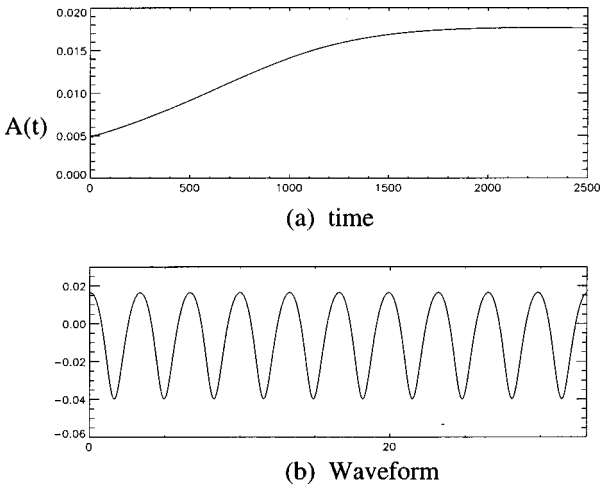

FIG. 15. A simulation of saturation for experiments of Ref. 9, $R_1=394$. (a) The maximum of interface amplitude against time. The saturation amplitude is about 0.0175. (b) The wave shape at time $t=2500$.

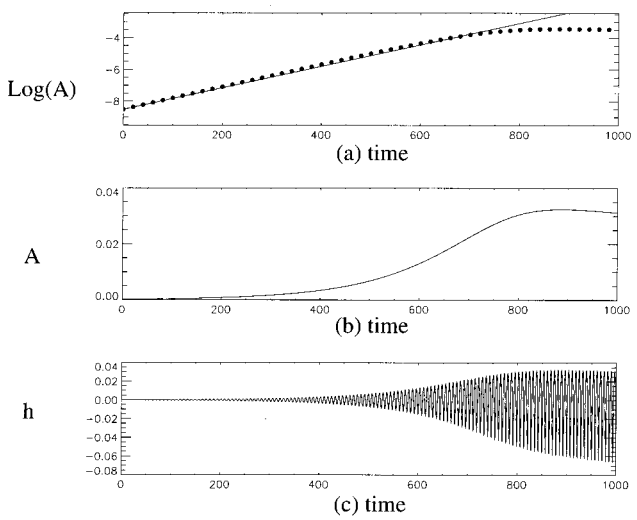

FIG. 16. The simulation of saturation for experiments of Ref. 9, $R_1=500$. (a) A log plot of the maximum of interface height; a solid line represents theoretical growth and circles represent the calculation. (b) A plot of the maximum of the interface position. (c) The perturbation interface height at $x=0$ against time. The calculation is carried out on a 256×256 mesh.

need to start from a very small perturbation amplitude to keep the flow in the linear regime for a long time. We set $A(0)=0.001$. At the top of Fig. 17, we plot, on a $\log_{10}$-linear scale, the evolution of the maximum amplitude $A(t)$ against the time. Until $t=100$, the numerical and theoretical growth rates agree, the difference between them being 2%, and the agreement zone is over one and a half decade. The evolution of the maximum of the vertical velocity V and L_2 norm against time are shown also in Fig. 17, and good agreement

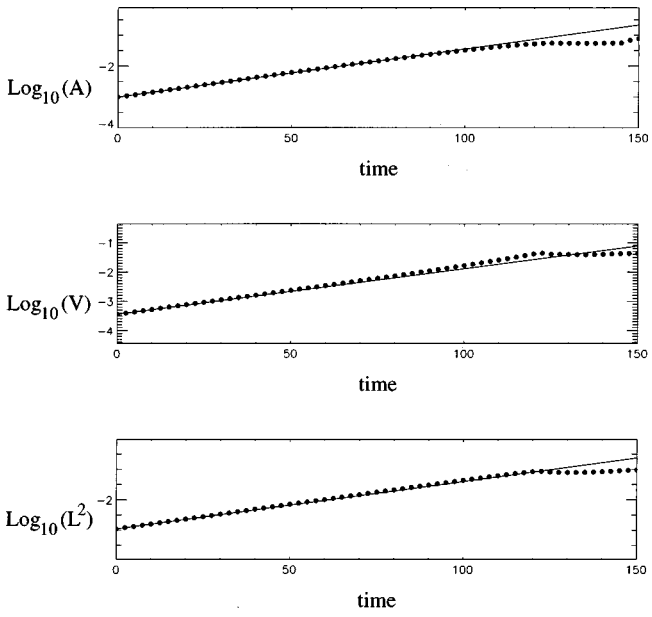

FIG. 17. Log plots of the maximum of interface position, the maximum vertical velocity V, and the L_2 norm against time for the flow: $A(0)=0.001$, $\alpha=\pi/2$, $R_1=500$, $m=0.5$, $l_1=0.372$, $T=0.01$, equal densities, and zero gravity. The theoretical linear growth rate for the interfacial mode is 0.035 77. Solid lines represents theoretical growth and circles represent the calculation. The calculation is carried out on a 256×256 mesh.

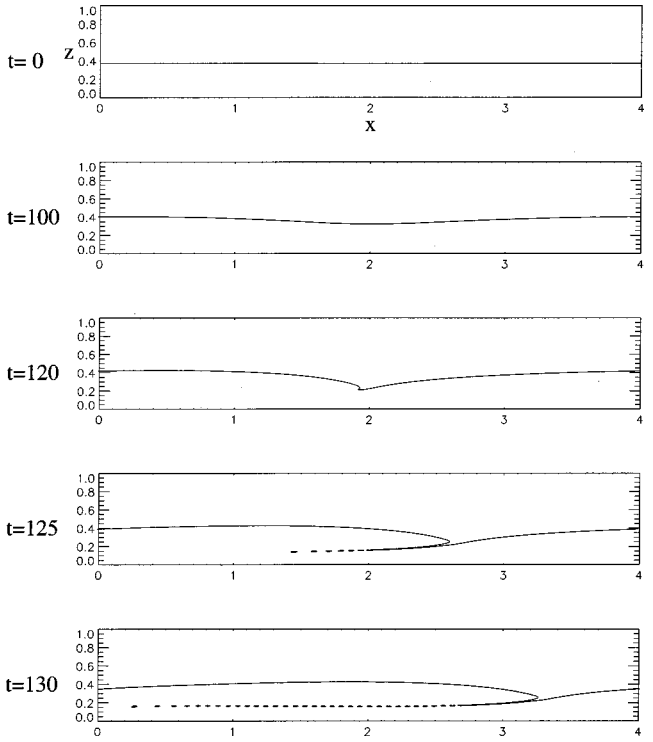

FIG. 18. The sequence of interface positions for $A(0)=0.001$, $\alpha=\pi/2$, $R_1=500$, $m=0.5$, $l_1=0.372$, $T=0.01$, equal densities, and zero gravity. Here $t=0$, 100, 120, 125, and 130. The calculation is carried out on a 256 $\times256$ mesh.

is also obtained. This calculation is carried out on a 256 $\times256$ mesh.

Corresponding to Fig. 17, we plot in Fig. 18 interface profiles for time $t=0$, 100, 120, 125, and 130. As the interface moves vertically under the viscosity-jump instability, the two fluids do not penetrate into each other in the same manner. Note that the upper fluid is more viscous than the lower one. We observe that at $t=100$, the interface trough is more narrow than interface crest and the interface loses its shape symmetry. At this stage, we can conclude already from mass conservation that the upper fluid penetrate faster into a lower fluid. This can be explained by the fact that the low-viscosity liquid provides less resistance, making it easier for the high-viscosity liquid to penetrate inside it. An analogy is that when inertia is important, a high-density fluid penetrates easily into a low-density fluid.

At time $t=120$, the upper fluid penetrates clearly into the lower one and the interface forms a fine finger. No finger formation can be seen in the upper fluid. Under the convection of the simple shear flow, this finger folds toward the right side, because the upper fluid moves fast than the lower one. The figure at time $t=125$ shows that the finger is elongated and breaks up, yielding a series of drops. From the figure for time $t=130$ and simulations for later times, we notice that these drops will not reach the bottom wall but return to the interface and consequently form a blob of the lower fluid sitting in the upper fluid. We should mention that fingers and drops in two-dimensional flow correspond to fluid sheets and columns in real flow.

We build on these results by varying the initial ampli-

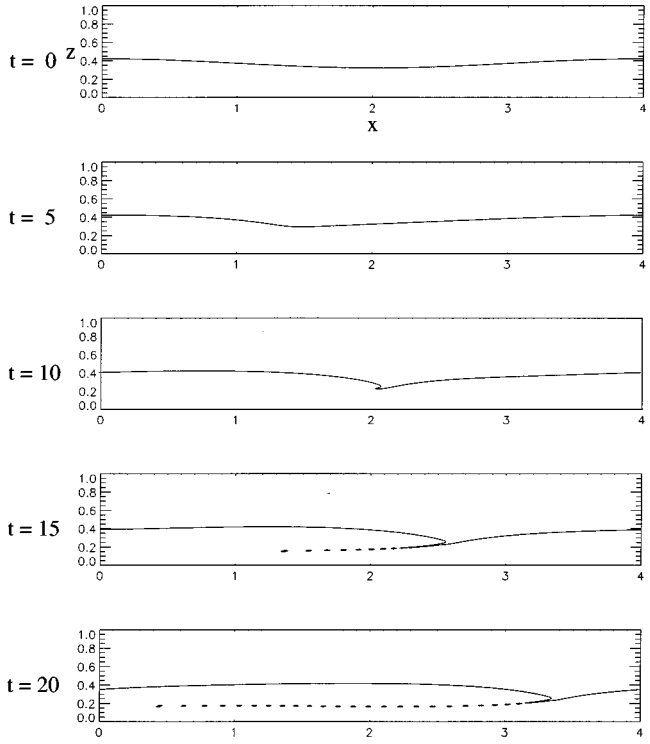

FIG. 19. The sequence of interface positions for $A(0)=0.05$, $\alpha=\pi/2$, $R_1=500$, $m=0.5$, $l_1=0.372$, $T=0.01$, equal densities, and zero gravity. Here $t=0$, 5, 10, 15, and 20. The calculation is carried out on a 256×256 mesh.

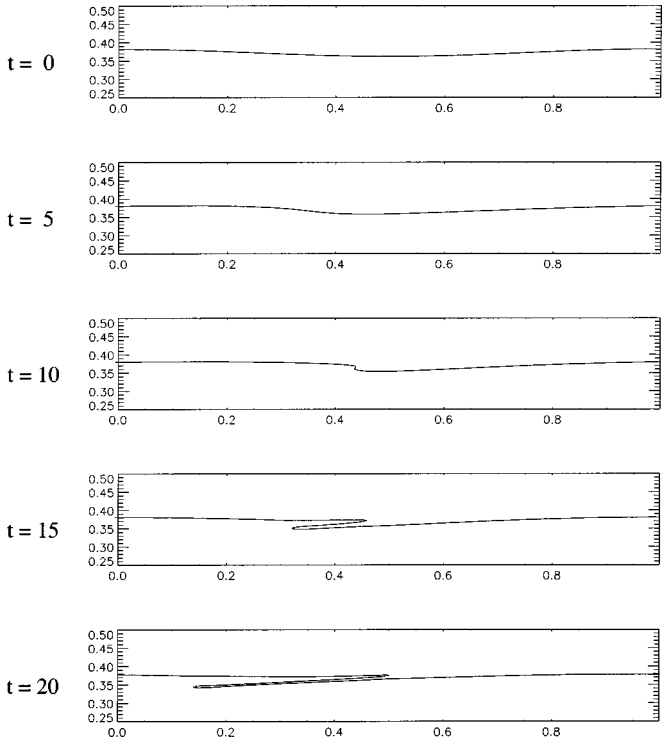

FIG. 20. The sequence of interface positions for $A(0)=0.01$, $\alpha=6.3$, $R_1=40$, $m=0.5$, $l_1=0.372$, $T=0.01$, equal densities, and zero gravity. Here $t=0$, 5, 10, 15, and 20. The calculation is carried out on a 160×320 mesh.

tude and the Reynolds number. First, it is interesting to investigate how changes in the initial amplitude affects the subsequent flow. Figure 19 illustrates $A(0)=0.05$, with the other parameters kept constant. This initial amplitude is 50 times larger than the previous value, and although small differences can be observed, the qualitative features of the previous flow are repeated; i.e., the plots shown in Fig. 18 now occur at time $t=0$, 5, 10, 15, and 20. In particular, from time $t=125$ to $t=130$ in Fig. 18 and from time $t=15$ to $t=20$ for $A(0)=0.05$ in Fig. 19, the time durations are both 5 s and the evolution of the two elongated fingers and the motion of the drops are almost identical. Mesh convergence is established on a 128×128 mesh, which uses half the number of points in the x and y directions of the previous investigation. Good agreement is obtained here also. It is crucial for 3-D computations to use the minimum number of points in a mesh in order to minimize computation time and at the same time to obtain information of good quality, because of memory limitation and computational cost. These two latter investigations suggest that we can study the three-dimensional problem for Reynolds number $R_1=500$ from a relative large initial amplitude (consequently reduce the computation time) and using a small mesh (consequently economize the memory) without losing important information of the flow subject to a small sinusoidal perturbation.

Second, we investigate the Couette flow for relatively low Reynolds numbers. A numerical investigation is carried out first for Reynolds number $R_1=40$ with wave number $\alpha=6.3$. We start the simulation from the initial amplitude $A(0)=0.01$. Figure 20 shows the interface profiles for time $t=0$, 5, 10, 15, and 20. This calculation is done on a 160×320 mesh. Asymptotic theory shows that the interface growth rate decreases as the Reynolds number decreases. For low Reynolds number flow, therefore, the convection of shear flow is the dominant mechanism that contributes to the evolution of the interface. At time $t=5$, the interface is already steepening, and at time $t=10$, the interface folds under the simple shear flow. Times $t=10$, $t=15$, and $t=20$ show only a finger in the lower fluid. From $t=10$ to $t=20$, the finger does not penetrate so much into the lower fluid but elongates in the streamwise direction. One striking fact compared to the flow with Reynolds number $R_1=500$ is that this finger rests on a straight line. Unlike the $R_1=500$ case where the wave number is $\pi/2$, we consider here a relative short wave with wave number 6.3. The finger head at time $t=15$ and $t=20$ is still far from the bottom wall. The perturbation grows very slowly according to linear theory and the whole velocity field is essentially the basic shear flow, which convects the finger along a straight line. The simulation is also carried out on a 160×256 mesh, where we observe that the above finger breaks up numerically due to lack of vertical refinement in the mesh; i.e., the 160×256 mesh is not fine enough to calculate this flow.

The identical flow with large initial amplitude $A(0)$ is investigated on a 160×160 mesh and the interface profiles for time $t=0$, 2, 5, 8, and 10 are plotted in Fig. 21. Since the initial amplitude is larger here, the influence of the basic shear flow is proportionately more evident. This flow shows a very different behavior than the flow with small initial amplitude. These two fingers are elongated more and more as time progresses.

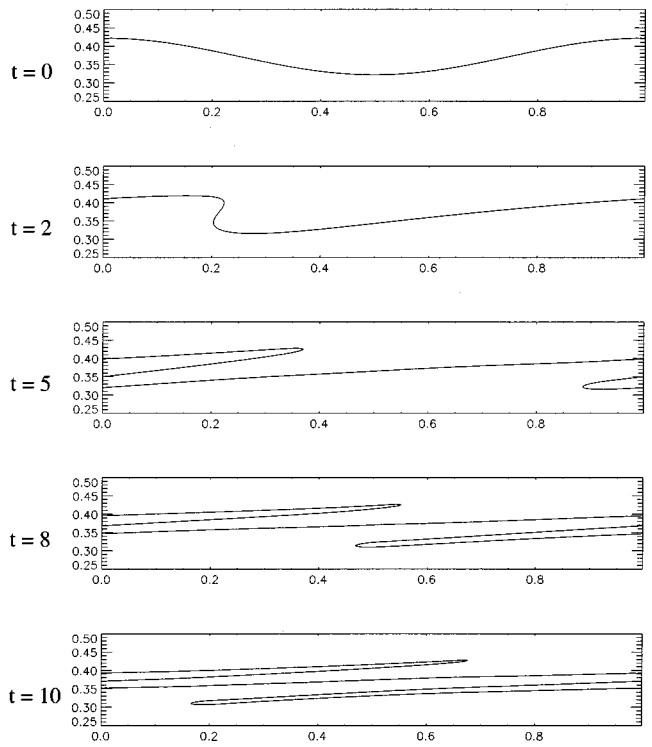

FIG. 21. The sequence of interface positions for $A(0)=0.05$, $\alpha=6.3$, $R_1=40$, $m=0.5$, $l_1=0.372$, $T=0.01$, equal densities, and zero gravity. Here $t=0$, 5, 10, 15, and 20. The calculation is carried out on a 160×160 mesh.

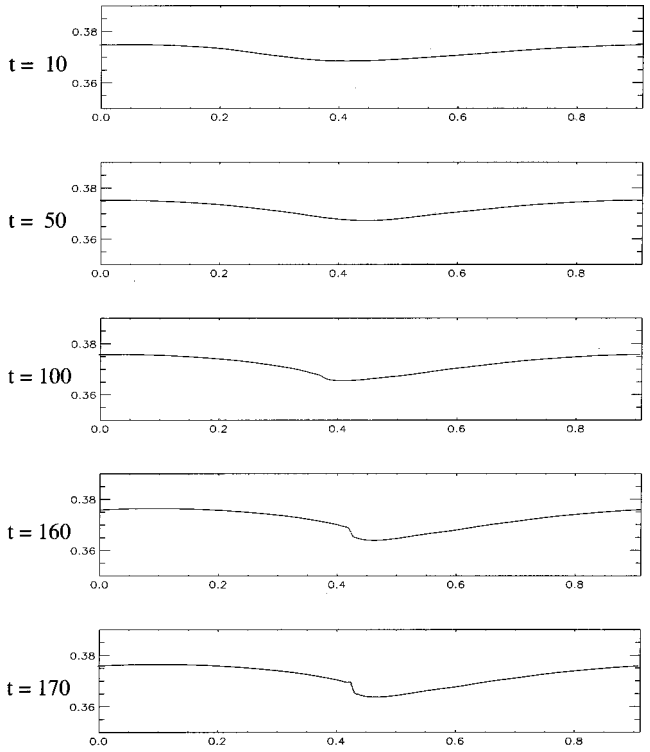

FIG. 22. The sequence of interface positions for $A(0)=0.003$, $\alpha=6.3$, $R_1=15$, $m=0.5$, $l_1=0.372$, $T=0.01$, equal densities, and zero gravity. Here $t=10$, 50, 100, 160, and 170. The calculation is carried out on a 256×320 mesh.

Finally, we investigate a low Reynolds number case with $R_1=15$. For this flow with wave number $\alpha=6.9$, linear theory predicts a growth rate 0.0089 (see Table I) and weakly nonlinear theory predicts the saturation amplitude $Z_0=0.0047$. We begin the simulation from initial amplitude $A(0)=0.003$, which is below the saturation amplitude. The practical constraint on the initial amplitude is that the weak growth rate due to linear theory results in longer computation times for smaller amplitudes. Figure 22 shows the interface profiles of our simulation on a 25×320 mesh. The time steps are $t=10$, 50, 100, 160, and 170. We should mention that we have enlarged the y direction scale to provide a better view due to the smallness of the wave amplitude. The growth rate here is five times smaller than the case with $R_1=40$, the vertical motion of the interface is so slow that the shear flow has enough time to shift the interface crest and trough significantly, despite the very small difference of the crest and trough height. Figure 22 for time $t=10$ and $t=50$ shows that the interface loses its initial sinusoidal shape because of the shifting of the wave crest and trough. The interface is no longer symmetrical. The additional fact that we observed in previous examples is that the crest is large and flat, while the trough is narrow. This suggests, as before, that the upper fluid penetrates fast into the lower one. As time goes on, the interface steepens further, as is evident from the wave forms shown at times $t=100$ and $t=160$. At $t=170$, the interface turns to fold near the trough like the the $R_1=40$ flow at $t=10$ in Fig. 20. The upper tip of the fold is, however, very fine, since with the 256×320 mesh only a small tip can be seen. Although we need a finer mesh to calculate well this interface folding, we can conclude from the interface shape in Fig. 22 and those not shown here for later times that this flow forms a finger. The examples shown in this section exhibit wave form folding with subsequent finger formation, even at fairly low amplitudes, indicating that the weakly nonlinear theory may have a smaller than expected region of applicability for low Reynolds number flow.

Similar shapes for two-dimensional fingers have been recorded in Fig. 3 of Ref. 27, where creeping flow is treated with the boundary integral method. At zero Reynolds number, the linear instability of the interface is absent, but with a sufficiently large-amplitude perturbation, a nonlinear evolution to fingering occurs from the following mechanism. With the base flow of Fig. 2, and with the initially sinusoidal interface as in Fig. 25 superposed, it is evident that the crest of the wave moves forward faster than the trough (see Fig. 23),

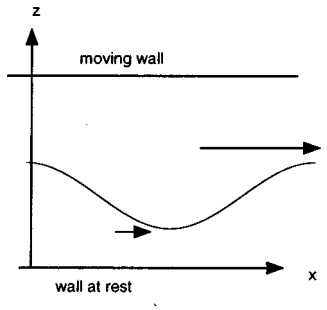

FIG. 23. The large-amplitude disturbance in creeping flow leads to fingering because the trough is left behind while the crest hurries on.

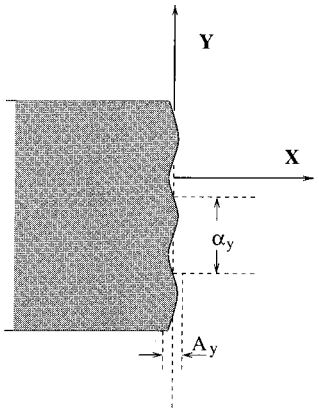

FIG. 24. Horizontal perturbation of the two layer flow.

and this motion initiates the fingering that is observed in Ref. 27. This is related to our situation, where on top of the low Reynolds numbers we address, we also have the instability due to inertial effects.

V. FINGERING IN THREE DIMENSIONS

The response to periodic perturbations in three dimensions is analyzed by using a horizontal undulation of the phase. The initial interface is

$$z = l_1 + A_x(0)\cos[\alpha_x x + \phi(y)], \tag{30}$$

$$\phi = A_y(0)\cos(\alpha_y y), \tag{31}$$

where $A_x(0)$ is the two-dimensional perturbation amplitude, $A_y(0)$ the spanwise perturbation amplitude, α_x the x-direction wave number, and α_y the y-direction wave number. Basically, the initial conditions are derived as follows: v is zero, and in each $x-z$ plane the velocity field (u,w) and the interface position are derived from the two-dimensional configuration. However, the phase of the cosine wave is shifted in the y direction (Fig. 24). This spanwise interface perturbation is used to provoke a three-dimensional instability. This perturbation formulation is inspired by the experiment of Lasheras and Choi[39] on the shear layer flow.

The two-dimensional fingering study in the previous section provides useful information for the subsequent three-dimensional investigation. As we have seen, small perturbations to low Reynolds number flow involves small interface structures and a fine mesh is needed to capture them. In addition, a three-dimensional simulation is limited by machine memory and compution time. In this section, we study only the flow with Reynolds number $R_1 = 500$. For this flow, the simulation with initial amplitude $A(0) = 0.05$ on a 128×128 mesh captures the flow characteristics sufficiently well. We have not yet studied the most unstable spanwise mode. We simply select $\alpha_y = 4\pi$ as the spanwise wavenumber. The three-dimensional calculation is therefore done in a box of size $4 \times 0.5 \times 1$ with a $128 \times 32 \times 128$ mesh, as in the previous section, the initial two-dimensional amplitude is $A_x(0) = 0.05$, for a flow with wave number $\alpha_x = \pi$, $R_1 = 500$, $m = 0.5$, $l_1 = 0.372$, $T = 0.01$. We use a spanwise amplitude $A_y(0) = 0.1$; thus the initial interface height is $z = 0.372 + 0.05\cos[\pi/2x + 0.1\cos(4\pi y)]$. The initial interface position is shown by Fig. 25. The finger is in the lower fluid, but we have reversed our three-dimensional visualization box, in order to provide a better view; the wave crest seen here corresponds to a trough.

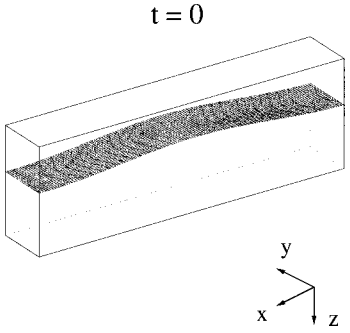

FIG. 25. The simulation of two-layer Couette flow for Reynolds number $R_1 = 500$, $\alpha = \pi/2$, $m = 0.5$, $l_1 = 0.372$, $T = 0.01$, equal densities, and zero gravity. The initial interface height is $z = 0.372 + 0.05\cos[6.3x + 0.1 \times \cos(y/4\pi)]$. The interface position is shown at $t = 0$.

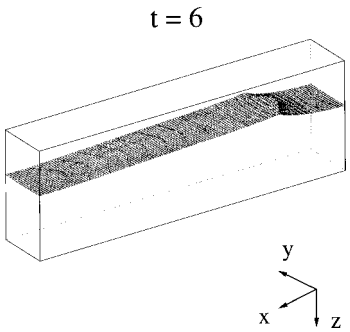

FIG. 26. The interface position is shown at $t = 6$. The interface begins to fold and the y-direction perturbation is amplified clearly near the trough.

Figures 26, 27, and 28 show interface shapes at $t = 6$, 10, and 12, respectively. The flow shows a quasi-two-dimensional character at $t = 6$; the three-dimensional effect is weak unless near the wave trough where the interface begins to fold and the transverse y-direction perturbation is clearly amplified. As in the two-dimensional case, we observe the formation of the finger in the low-viscosity fluid for $t = 10$. The thin sheet that is formed is reminiscent of the two-dimensional cusp-like fingering of Fig. 2. In addition to this, we observe that this three-dimensional finger is longer than

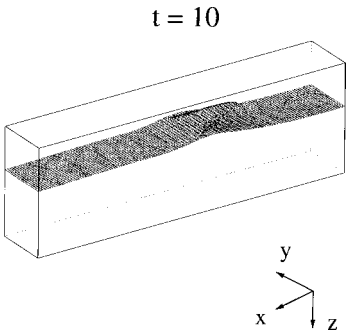

FIG. 27. The interface position is shown at $t = 10$. The formation of a finger in lower-viscosity fluid. This finger is longer than the one in the two-dimensional case at the same time.

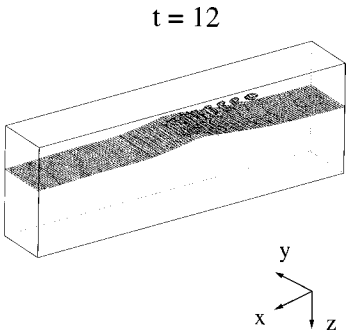

FIG. 28. The interface position is shown at $t=12$. The three-dimensional finger breaks up, yielding a series of drops in the low-viscosity fluid.

the two-dimensional case of the previous section for this time. This is due to the three-dimensional effects of the perturbed flow. Finally, for $t=12$, this finger breaks up yielding a series of drops in the low-viscosity fluid.

VI. CONCLUSION

We have explored the evolution of linear disturbances, the weakly nonlinear regime, saturation to spatially periodic traveling waves, and fingering of large-amplitude periodic disturbances. In order to achieve the computational results, we have implemented a semi-implicit scheme to enable faster computations at low Reynolds numbers, and a second-order velocity interpolation for greater accuracy of the interface advection. We have shown the development of elongated fingers, which allow the migration of the more viscous into the less viscous liquid, and vice versa, depending on the fluid parameters. These fingers break up when perturbed in three dimensions, and form droplets reminiscent of Fig. 1.

ACKNOWLEDGMENT

This research was sponsored by the National Science Foundation under Grants No. CTS-9612308 and No. DMS-9622735. J. Li thanks his Ph.D. advisor Professor Zaleski for introducing him to two phase flows.

[1]C-S. Yih, ''Instability due to viscosity stratification,'' J. Fluid Mech. **26**, 337 (1967).
[2]D. D. Joseph, K. Nguyen, and G. Beavers, ''Non-uniqueness and stability of the configuration of flow of immiscible fluids with different viscosities,'' J. Fluid Mech. **141**, 319 (1984).
[3]K. Chen, ''Interfacial instabilities in stratified shear flows involving multiple viscous and viscoelastic fluids,'' Appl. Mech. Rev. **48**, 763 (1995).
[4]D. D. Joseph, ''Steep wave fronts on extrudates of polymer melts and solutions: lubrication layers and boundary lubrication,'' J. Non-Newtonian Fluid Mech. **70**, 187 (1997).
[5]Y. Renardy, ''Instability at the interface between two shearing fluids in a channel,'' Phys. Fluids **28**, 3441 (1985).
[6]Y. Renardy, ''Weakly nonlinear behavior of periodic disturbances in two-layer Couette–Poiseuille flow,'' Phys. Fluids A **1**, 1666 (1989).
[7]A. V. Coward, Yuriko Renardy, M. Renardy, and J. R. Richards, ''Temporal evolution of periodic disturbances in two-layer Couette flow,'' J. Comput. Phys. **132**, 346 (1997).
[8]P. Barthelet and F. Charru, ''Experimental study of interfacial waves in a two-layer shear flow: short wave modulations and long wave–short wave interactions,'' in *Advances in Multi-Fluid Flows*, edited by Y. Renardy, A. V. Coward, D. Papageorgiou, and S. M. Sun (SIAM, Philadelphia, 1996), pp. 13–41.
[9]P. Barthelet and F. Charru, ''Benjamin-Feir and Eckhaus instabilities with Galilean invariance: the case of interfacial waves in viscous shear flows,'' Eur. J. Mech. B/Fluids **17**, 1 (1998).
[10]J. R. Richards, A. N. Beris, and A. M. Lenhoff, Phys. Fluids **7**, 2617 (1995).
[11]R. W. Yeung, Annu. Rev. Fluid Mech. **14**, 395 (1982).
[12]S. O. Unverdi and G. Tryggyason, ''A front-tracking method for viscous, incompressible, multi-fluid flows,'' J. Comput. Phys. **100**, 25 (1992).
[13]S. Osher and J. A. Sethian, ''Fronts propagating with curvature-dependent speed: algorithms based on Hamilton–Jacobi formulations,'' J. Comput. Phys. **79**, 12 (1988).
[14]FLOW-3D Users Manual, Flow Science, Inc., Los Alamos, NM, 1988.
[15]B. Lafaurie, C. Nardone, R. Scardovelli, S. Zaleski, and G. Zanetti, ''Modeling merging and fragmentation in multiphase flows with SURFER,'' J. Comput. Phys. **113**, 134 (1994).
[16]B. D. Nichols, C. W. Hirt, and R. S. Hotchkiss, ''SOLA-VOF: A solution algorithm for transient fluid flow with multiple free boundaries,'' Los Alamos Scientific Laboratory Report LA-8355, 1980.
[17]D. B. Kothe, R. C. Mjolsness, and M. D. Torrey, ''RIPPLE: A computer program for incompressible flows with free surfaces,'' Los Alamos National Laboratory Report No. LA-12007-MS, 1991.
[18]S. Zaleski, J. Li, and S. Succi, ''Two-dimensional Navier-Stokes simulation of deformation and breakup of liquid patches,'' Phys. Rev. Lett. **75**, 244 (1995).
[19]W. F. Noh and P. Woodward, ''The SLIC (simple line interface calculation) method,'' Lawrence Livermore Laboratory Report No. UCRL-52111, 1976.
[20]C. W. Hirt and B. D. Nichols, ''Volume of fluid VOF for the dynamics of free boundaries,'' J. Comput. Phys. **39**, 201 (1981).
[21]J. U. Brackbill, D. B. Kothe, and C. Zemach, ''A continuum method for modeling surface tension,'' J. Comput. Phys. **100**, 335 (1992).
[22]J. Li, ''Résolution numérique de l'équation de Navier–Stokes avec reconnexion d'interfaces. Méthode de suivi de volume et application à l'atomisation,'' Ph.D. thesis, Université Pierre et Marie Curie, 1996.
[23]S. Popinet and S. Zaleski, ''A front tracking algorithm for the accurate representation of surface,'' submitted to Int. J. Numer. Methods Fluids.
[24]D. Gueyffier, J. Li, A. Nadim, R. Scardovelli, and S. Zaleski, ''Volume of fluid interface tracking and smoothed surface stress methods applied to multiphase flow and pendant drop pinching,'' submitted to J. Comput. Phys.
[25]J. Li, ''Calcul d'interface affine par morceaux,'' C. R. Acad. Sci. Paris **320**, 391 (1995).
[26]F. X. Keller, J. Li, A. Vallet, D. Vandromme, and S. Zaleski, ''Direct numerical simulation of interface breakup and atomisation,'' *Proceedings of the Sixth International Conference on Liquid Atomization and Spray Systems*, edited by A. J. Yule and C. Dumouchel (1994), pp. 56–62.
[27]C. Pozrikidis, ''Instability of two-layer creeping flow in a channel with parallel sided walls,'' J. Fluid Mech. **351**, 139 (1997).
[28]A. J. Chorin, ''A numerical method for solving incompressible viscous flow problems,'' J. Comput. Phys. **2**, 12 (1967).
[29]F. H. Harlow and J. E. Welsh, ''Numerical calculation of time-dependent viscous incompressible flow with a free surface,'' Phys. Fluids **8**, 2182 (1965).
[30]Y. Zang, R. L. Street, and J. R. Koseff, ''A non-staggered grid, fractional step method for time-dependent incompressible Navier–Stokes equations in curvilinear coordinates,'' J. Comput. Phys. **114**, 18 (1994).
[31]R. Peyret and T. D. Taylor, *Computational Methods for Fluid Flow* (Springer-Verlag, Berlin, 1990).
[32]R. DeBar, ''Fundamentals of the KRAKEN code,'' Technical Report No. UCIR-760, LLNL, 1974.
[33]A. J. Chorin, ''Flame advection and propagation algorithms,'' J. Comput. Phys. **35**, 1 (1980).
[34]D. L. Youngs, ''Time-dependent multi-material flow with large fluid distortion,'' in *Numerical Methods for Fluid Dynamics*, edited by K. W. Morton and M. J. Baines (Academic, New York, 1982), pp. 273–285.
[35]D. B. Kothe and W. J. Rider, ''Comments on modelling interfacial flows with volume-of-fluid methods,'' submitted to J. Comput. Phys.
[36]E. G. Puckett, A. S. Almgren, J. B. Bell, D. L. Marcus, and W. J. Rider, ''A higher order projection method for tracking fluid interfaces in variable density incompressible flow,'' J. Comput. Phys. **130**, 269 (1995).
[37]R. Scardovelli (private communication).
[38]P. A. M. Boomkamp, ''Weakly nonlinear stability of parallel two-phase flow: comparison with experiments,'' preprint, 1998.
[39]J. C. Lasheras and H. Choi, ''Three-dimensional instability of a plane free shear layer: an experimental study of the formation and evolution of streamwise vortices,'' J. Fluid Mech. **189**, 53 (1988).